Frequency-modulated high-power photonic-crystal surface-emitting lasers for long-distance coherent free-space optical communications

Takuya Inoue [1,6] ✉, Ryohei Morita[2,6], Shota Ishimura [3], Shuei Nakano[2], Hidenori Takahashi [3], Takehiro Tsuritani[3], Menaka De Zoysa [1], Kenji Ishizaki[1], Masatoshi Suzuki [4] & Susumu Noda [1,5] ✉

High-power coherent optical transmitters with high-speed controllability are in demand for a number of cutting-edge applications, including intersatellite communications and deep-space optical communications. The conventional transmitters used in these applications require many bulky optical components besides their semiconductor laser sources, such as fibre-optical amplifiers, external phase modulators, optical fibres and beam-collimation lenses, which are obstacles in achieving compact and efficient systems. Here we propose and experimentally demonstrate compact coherent optical transmitters based on frequency-modulated photonic-crystal surface-emitting lasers (PCSELs) towards achieving long-distance free-space optical (FSO) communications. We design two-section PCSELs that incorporate two photonic crystals with slightly different band-edge resonant frequencies, and we realize watt-class frequency modulation with suppressed amplitude modulation via anti-phase current injection into the two sections. Using the above two-section PCSELs as coherent optical transmitters, we demonstrate fibre-amplifier-free FSO communications with Gbps-class bandwidth, even when the laser power is attenuated by >80 dB. Our work opens avenues toward the realization of one-chip coherent optical transmitters whose volume and weight are several orders of magnitude smaller than conventional bulky systems for a wide variety of coherent free-space laser applications.

Single-mode semiconductor lasers are used for various applications that require optical coherence, including optical communications and optical metrology[1–4]. Recently, the range of applications for coherent semiconductor lasers has expanded further to include terrestrial free-space optical (FSO) communications and intersatellite optical communications between low Earth orbits (LEOs) and/or geostationary Earth orbits (GEOs)[5–8]. In these emerging applications, both laser monochromaticity and high-power (greater than watt-level) operation are required, and

coherent signal generation using techniques such as frequency modulation (FM) and phase modulation (PM) are also demanded to enable detection with high sensitivity for long-distance communications. Conventional single-mode semiconductor lasers, however, cannot afford such high output power while maintaining single-mode operation, and they typically use an external phase modulator to generate FM or PM signals. Accordingly, conventional high-power coherent transmission systems require a number of bulky optical components, such as fibre-optical
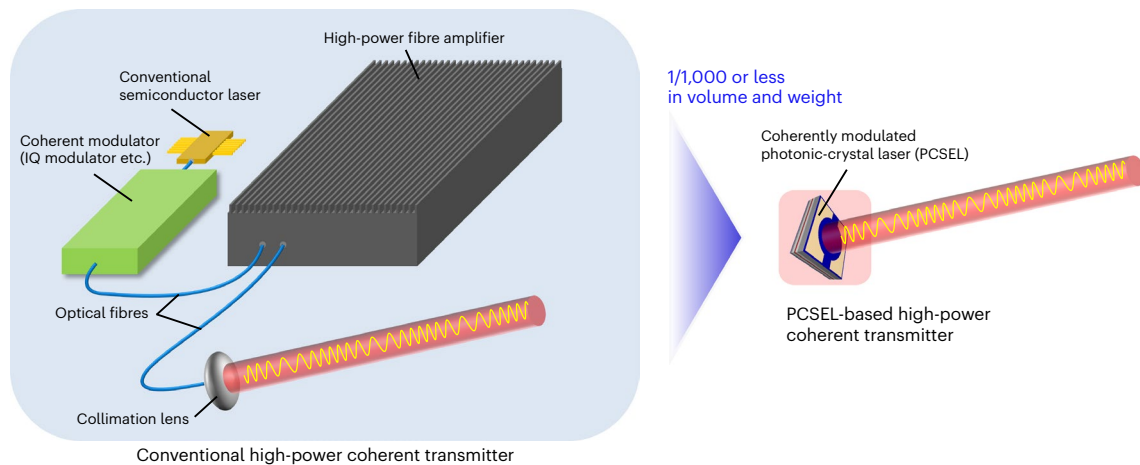
Fig. 1 | Concept of the PCSEL-based high-power coherent transmitter. Progression from conventional high-power coherent transmission systems (left) to the PCSEL-based high-power coherent transmitter (right).

amplifiers with relatively low electro-optical conversion efficiency, external phase modulators, single-mode fibres and beam-collimation lenses (shown in the left part of Fig. 1), which undermines the advantages of compactness and the high efficiency of the semiconductor lasers.

Photonic-crystal surface-emitting lasers (PCSELs) are considered to be a leading candidate to satisfy the above requirements without forfeiting the advantages of semiconductor lasers, because PCSELs can realize single-mode high-power lasing over a large emission area owing to a two-dimensional coherent band-edge resonance inside the photonic-crystal layer[9–17]. General design guidelines have already been established to maintain single-mode oscillation with large-area PCSELs[14], and the experimentally achieved single-mode output power has increased from 1–10 W to 50 W by enlarging the device diameter of the PCSEL from 0.5–1 mm (ref. 12) to 3 mm (ref. 15). In addition, owing to the accumulation of a much larger number of photons inside these large-area PCSELs compared to conventional semiconductor lasers, PCSELs can also realize narrow intrinsic spectral linewidths (less than kilohertz) without relying on any optical feedback systems[17]. Thanks to these features, PCSELs are promising candidates for one-chip high-power coherent transmitters, as schematically shown in the right panel of Fig. 1. However, the method to realize high-speed coherent modulation (FM or PM) in PCSELs, which is essential to enable high-sensitivity coherent detection harnessing the advantage of narrow-linewidth PCSELs, has yet to be clarified.

In this Article we propose and experimentally demonstrate PCSELs that enable high-power FM with suppressed amplitude modulation (AM) under direct modulation, and we apply these PCSELs to coherent FSO transmitters. We propose two-section PCSELs that incorporate two photonic crystals with slightly different lattice constants, and we realize watt-class FM signals with a gigahertz-class bandwidth while suppressing AM signals. Then, by using one such two-section PCSEL as a transmitter, we demonstrate coherent Gbps-class FSO communication with an allowable power attenuation (or link budget) of >80 dB in an optical-amplifier-free transmitter configuration. Our work is an important milestone towards the realization of one-chip coherent FSO transmitters whose volumes and weights are several orders of magnitude smaller than those of conventional, bulkier systems. Such compact transmitters are expected to find favour in various fields of space communication, including ground-to-satellite, intersatellite (LEO–GEO), Moon-to-Earth and deep-space communications.

Results
Proposal of two-section PCSELs for the generation of FM signals

Figure 2a presents a schematic of a two-section PCSEL for the generation of large FM signals. Here, double-lattice photonic crystals

with slightly different lattice constants ($a = a_0 \pm \Delta a/2$, $a_0 = 276$ nm, $\Delta a/a_0 = 8 \times 10^{-5}$) are introduced inside the current injection region (diameter of 500 μm), whereby a small difference in the band-edge frequency ($\Delta f_{12} = 26$ GHz) is introduced between the two sections (PC1 and PC2). The top-side electrodes above the two sections are also divided to enable the injection of different amounts of current (I_1, I_2). The detailed structures of the PCSEL and double-lattice photonic crystal are provided in Supplementary Section 1. Figure 2b presents a schematic of the band-edge frequency distribution and calculated photon distributions inside the device (the numerical simulation method is detailed in Supplementary Section 2). By appropriately designing the coupling coefficients of the double-lattice photonic crystal, the light can be distributed in both sections, even when the band-edge frequency difference between the two PCs exists (Supplementary Section 3 provides details). When the injection current of PC1 becomes larger than that of PC2, the photon density inside PC1 increases, which induces a blueshift of the lasing frequency. On the other hand, when the injection current of PC2 becomes larger than that of PC1, the photon density inside PC2 increases, which induces a redshift of the lasing frequency. Therefore, by injecting anti-phase radiofrequency (RF) current with the same amount of bias current into the two sections as shown in Fig. 2c, the photon density of each section can be temporally modulated and the lasing frequency can be modulated in proportion to their difference. Moreover, as the sum of the injection current into the two sections is constant for the anti-phase modulation, AM signals can be suppressed in the proposed two-section device. This is different from conventional single-section PCSELs, which mainly induce intensity modulation[18–20].

To confirm the above-mentioned principle, we numerically simulated the FM and AM characteristics of the proposed two-section PCSELs by using time-dependent three-dimensional coupled-wave theory[21,22]. The calculated changes in lasing frequency and output power of the designed PCSEL for anti-phase sinusoidal modulation (bias current, $I_{dc} = 3.0$ A; RF current, $I_{rf} = 0.1$ A; modulation frequency, $f_{mod} = 1$ GHz) are shown in Fig. 2d. Here, we define the amplitude of the anti-phase RF current I_{rf} as that of the RF current injected into the active layer just above PC1/PC2, which is not always the same as that applied at the separated top electrodes (Supplementary Section 4 provides details). In the proposed device, a relatively large frequency change of 0.7 GHz$_{pp}$ is obtained while maintaining a small AM modulation depth ($m_a < 0.02$), which is defined as the ratio of the change in output power over the average power. We have also confirmed that there is no significant change in the beam profile during FM operation (Supplementary Section 5 provides details). Figure 2e,f shows the calculated changes in frequency (FM) and output power (AM) under direct sinusoidal modulation for the two-section PCSEL and
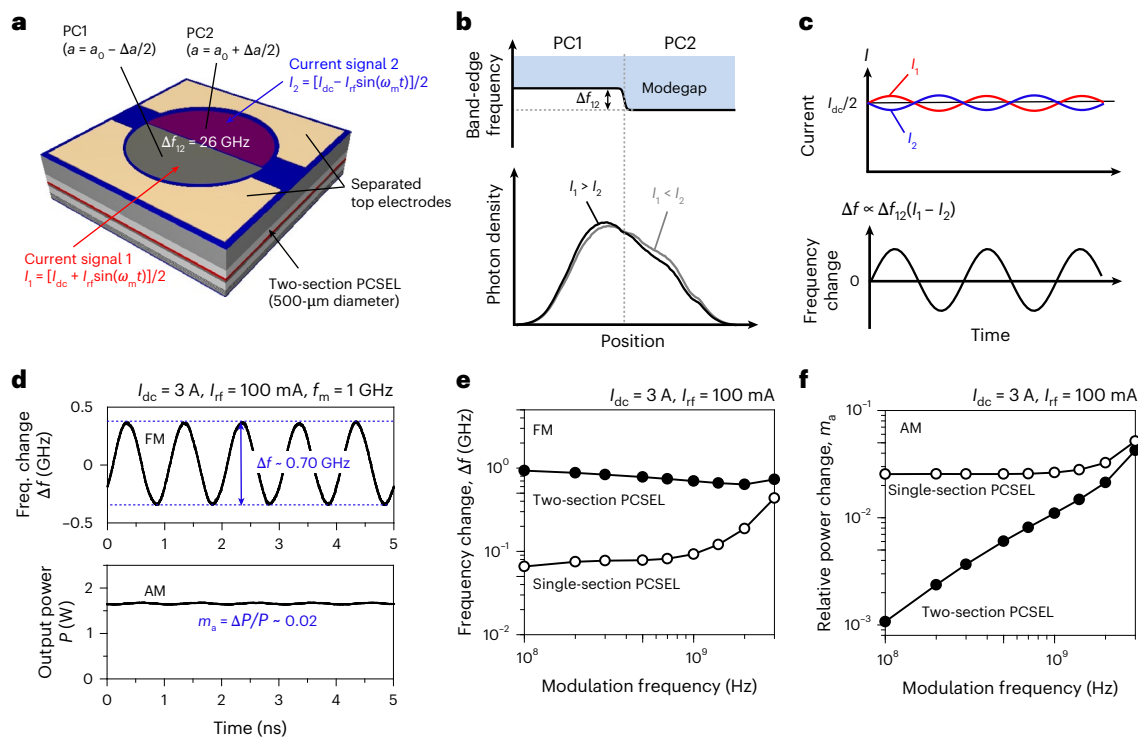
Fig. 2 | Principle and numerical results of two-section PCSELs for the generation of high-power FM signals. a, Schematic of the proposed two-section PCSEL. ω_m, angular frequency of modulation; t, time. **b**, Band-edge frequency and photon distributions inside the device. **c**, Principle of FM signal generation for anti-phase current modulation. **d**, Calculated temporal change in the lasing frequency (freq.) and output power of the two-section PCSEL under anti-phase sinusoidal current modulation. **e,f**, Calculated changes in frequency (FM) (**e**) and output power (AM) (**f**) under direct sinusoidal modulation for the two-section PCSEL and a single-section PCSEL as a function of the modulation frequency. In these calculations, the double-lattice photonic-crystal structure and modulation parameters ($I_{dc} = 3.0$ A, $I_{rf} = 0.1$ A) are assumed to be the same for both devices.

a conventional single-section PCSEL as functions of the modulation frequency. In these calculations, the photonic-crystal structure and modulation parameters ($I_{dc} = 3.0$ A, $I_{rf} = 0.1$ A) are assumed to be the same for both devices. These results show that the two-section PCSELs can realize a change of frequency that is one order of magnitude larger than the single-section PCSEL with the same amount of RF current I_{rf} with a suppressed AM component at modulation frequencies of up to 3 GHz, which corresponds to the relaxation frequency of the PCSEL. It should be noted that the AM response of the two-section PCSEL increases as the modulation frequency approaches the relaxation oscillation frequency, which is due to incomplete cancellation of the photon density change inside PC1 and PC2 at high modulation frequencies (Supplementary Section 6 provides details).

Demonstration of watt-class FM signal generation from two-section PCSELs

Based on the above design, we fabricated a two-section PCSEL with a lasing diameter of 500 μm and a lasing wavelength of 942 nm. Figure 3a presents a photograph of the fabricated two-section PCSEL, which was mounted on a cooling package. The two top-side electrodes on the PCSEL were wire-bonded to the external coplanar electrical circuits with a 50-Ω impedance, as shown in the figure. Figure 3b shows the measured current–light output (I–L) characteristics and far-field beam pattern of the fabricated device when the anti-phase RF current was not applied. An output power of >1 W was obtained at a bias current of 3 A, and single-mode lasing with a beam divergence angle of 0.2° ($M^2 \approx 1.6$), evaluated at $1/e^2$ of the maximum value, was realized. Figure 3c presents a schematic of the optical set-up utilized to measure the FM characteristics of the PCSEL. Here we generated an anti-phase RF current signal by using the differential output of an arbitrary waveform generator (AWG) and a broadband RF amplifier, and we directly modulated the PCSEL by

superimposing the bias current I_{dc} and the above anti-phase RF signal with a bias tee. We then mixed the light from the modulated PCSEL with that from a reference single-mode PCSEL to perform a heterodyne measurement. The heterodyne offset frequency of the two PCSELs before modulation was set to ~6 GHz by finely adjusting the temperature of the reference PCSEL. The beat note signals were acquired with a balanced photodetector (BPD) composed of two 42-GHz photodetectors (RXM42AF, Thorlabs) and were recorded with a real-time digital oscilloscope. Finally, the temporal change of the heterodyne beat note frequency was calculated (details are provided in Methods). We also measured the AM characteristics of the same device by directly measuring the amplitude change using another high-speed photodetector.

Figure 3d shows the measured FM and AM characteristics of the two-section PCSEL at a bias current of 3 A ($P_{ave} = 1.1$ W), an applied anti-phase RF current of ~0.22 A_{pp} and a modulation frequency of 1 GHz. We obtained an FM signal with a large frequency change of ~0.55 GHz$_{pp}$, while suppressing the modulation depth of the AM signal, m_a, below 0.1. Figure 3e,f shows the experimentally measured FM and AM changes under direct sinusoidal modulation for the two-section PCSEL as a function of the modulation frequency. In these graphs, we also plot the measured FM and AM characteristics of a conventional single-section PCSEL with the same amplitude of the applied RF current (0.22 A_{pp}) (Supplementary Section 7 provides details). Note that the measured values of the frequency change and the amplitude change contain several irregular variations, which might be caused by multiple reflections of the electrical signals due to impedance mismatching between the PCSEL and the coplanar electrical circuit. Excluding such effects, the frequency change Δf of the two-section PCSEL was twice as large as that of the single-section PCSEL at all modulation frequencies up to 1 GHz, and the amplitude modulation depth, m_a, of the two-section PCSEL was suppressed by a factor of 4. Using the ratio of FM/AM amplitude
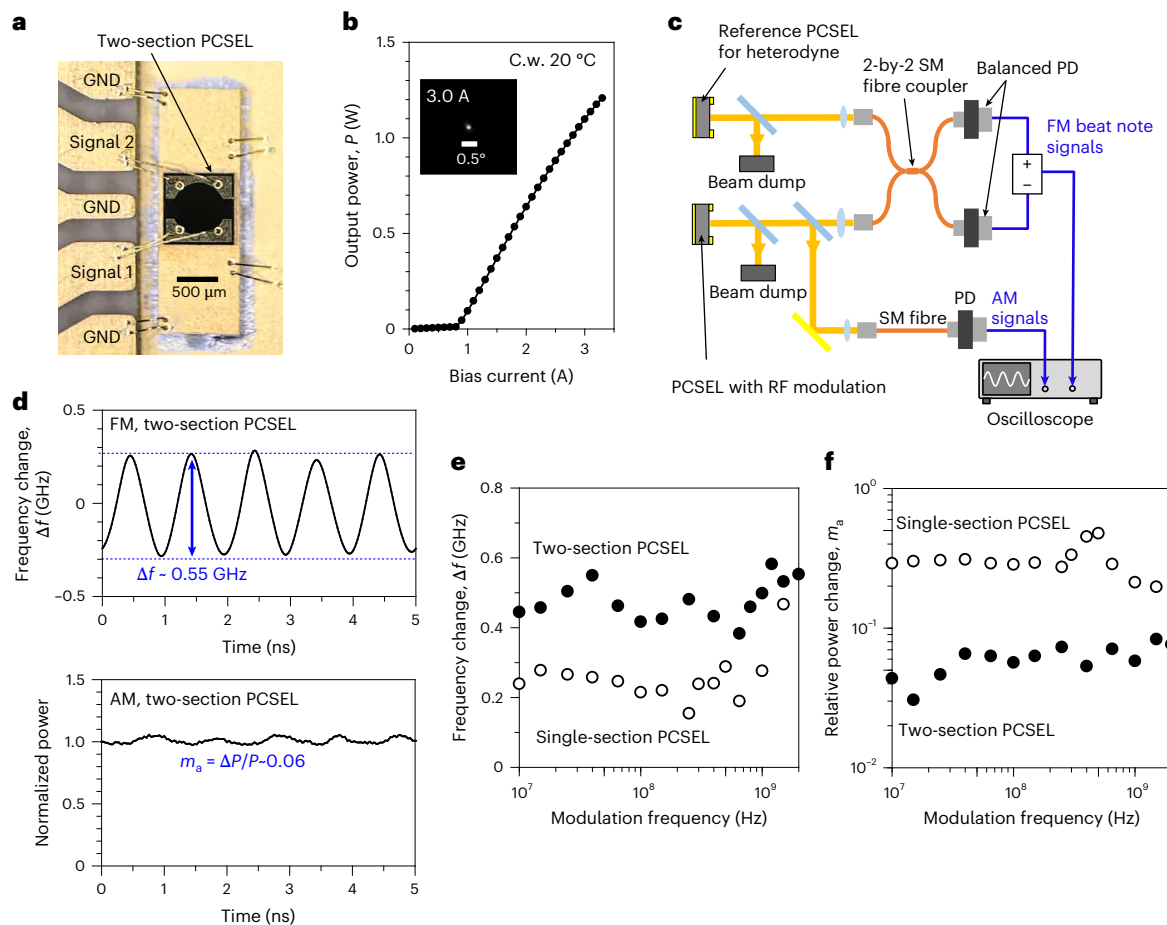
Fig. 3 | Measured FM and AM characteristics of fabricated two-section PCSELs.
a, Photograph of the fabricated two-section PCSEL, which was mounted on a cooling package. GND, ground. **b**, Measured $I–L$ characteristics and far-field beam pattern. C.w., continuous wave. **c**, Schematic of the optical set-up used to measure the FM and AM characteristics of the PCSELs. PD, photodetector; SM, single-mode. **d**, Measured temporal change of the lasing frequency and output power of the two-section PCSEL under anti-phase sinusoidal current modulation at a bias current of 3 A ($P_{ave} = 1.1$ W), an applied anti-phase RF current of 0.22 A_{pp} and a modulation frequency of 1 GHz. **e,f**, Measured changes in frequency (**e**, FM) and amplitude (**f**, AM) under direct sinusoidal modulation for the two-section PCSEL and the single-section PCSEL as functions of the modulation frequency.

($\Delta f/m_a$) as a figure of merit (FoM), the two-section PCSEL was seen to achieve a FoM that was one order of magnitude larger than that of the single-section PCSEL. Therefore, the two-section PCSEL was confirmed to enable the generation of watt-class FM signals with suppressed AM, which is suitable for coherent FSO communications with minimal AM noise. It should be noted that the measured two-fold enhancement of the frequency change in the two-section PCSELs is smaller than the calculated ten-fold enhancement predicted in the previous simulation. This is because the effective anti-phase RF current injected into the active layer was much smaller than that applied at the top-side (n-side) electrodes (Supplementary Section 4 provides details). By employing separated electrodes in the bottom side (p-side) instead of the top side, the effective anti-phase RF current injected into the active layer is expected to be substantially enhanced, enabling a ten-fold enhancement of the frequency change as predicted in the simulation.

Demonstration of optical-amplifier-free coherent FSO communications using FM PCSELs

Using the above two-section PCSEL, we performed a proof-of-concept demonstration of optical-amplifier-free coherent FSO communications. The experimental set-up is shown in Fig. 4a. Bipolar non-return-to-zero (NRZ) signals filtered by the raised-cosine filter were generated from the AWG and injected into the PCSELs using a bias tee after being amplified to 0.22 A_{pp}. The bias current of the PCSEL was set to 3.0 A, which corresponds to an output power of 1.1 W (30 dBm). Signal baud rates

of 0.5 Gbaud and 1 Gbaud were used. The watt-class FM signals emitted into free space from the PCSEL were attenuated by beamsplitters and a variable neutral density (ND) filter to emulate the link loss between a transmitter and receiver in practical long-distance FSO communications. After passing through the link-loss emulator, the optical signal was coupled into a single-mode fibre, and heterodyne beat note signals were obtained by using another reference PCSEL as a local oscillator (LO), as described in the previous sections. The optical power of the LO was maintained at 10 dBm. In this experiment, a different BPD that had a smaller electrical bandwidth (2.5 GHz), but lower electrical noise intensity, was used (PDB482C-AC, Thorlabs), and thus the heterodyne offset frequency between the two PCSELs was set to ~1 GHz, accordingly. The electrical signal from the BPD was recorded using a digital oscilloscope and finally processed by an offline digital signal processor. The above process was repeated by changing the amount of attenuation in the link-loss emulator (or the received signal power), and the bit-error ratios (BERs) of the FSO communications were evaluated for each link loss. Details of the BER evaluation and eye-diagram measurements are provided in Methods.

Figure 4b shows a measured eye diagram at a received power of −50 dBm and a signal baud rate of 0.5 Gbaud. The horizontal and vertical axes denote the time and the instantaneous frequency change of the laser, respectively. Despite the substantially large power attenuation at the link-loss emulator (80 dB), a clear eye pattern was observed, and a BER of below 5×10^{-5} (corresponding to the error-free transmission
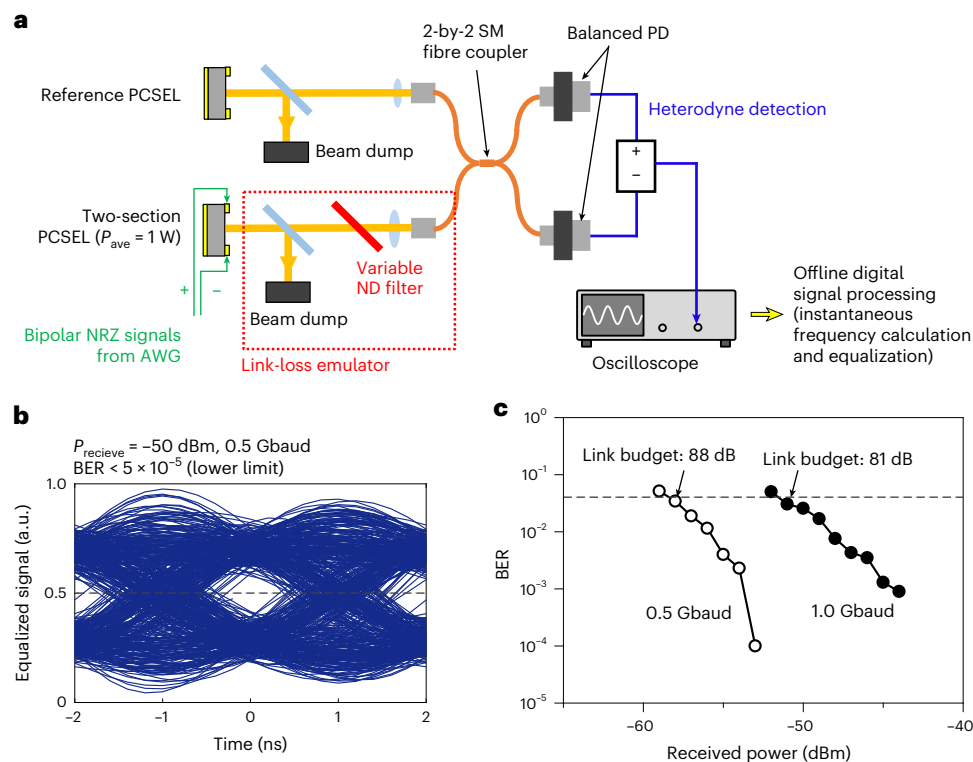
Fig. 4 | Demonstration of coherent FSO communications using two-section PCSELs. a, Schematic of the optical set-up for coherent FSO communications, comprising a two-section PCSEL, a link-loss emulator and a heterodyne receiver with a reference PCSEL as a local oscillator. **b**, Measured eye diagram at a received power of −50 dBm and a signal baud rate of 0.5 Gbaud. **c**, Measured BER of the coherent FSO communications when the received power was varied. The minimum allowable received optical power was −58 dBm and −51 dBm at 0.5 Gbaud and 1.0 Gbaud, respectively, corresponding to allowable power attenuations (link budgets) of 88 dB and 81 dB, respectively.

in this measurement) was achieved. Figure 4c shows the measured BER of the coherent FSO communication when the received power was varied. Assuming a BER threshold of 20% overhead soft-decision forward-error correcting code[23] (dashed line in Fig. 4c), the minimum allowable received optical power was −58 dBm and −51 dBm at 0.5 Gbaud and 1.0 Gbaud, respectively, corresponding to allowable power attenuations (link budgets) of 88 dB and 81 dB, respectively. The relatively large difference of ~7 dB between the two cases may be attributed to the limited electrical bandwidth of the BPD used in the experiment (2.5 GHz). Specifically, the high-order sidebands of the FM beat note signals may have become cut off at 1.0 Gbaud. It should also be noted that the above-mentioned received powers (<−50 dBm) and link budgets (>80 dB) are comparable to those required in long-distance intersatellite communications between GEO and ground or between GEO and LEO[24,25], which suggests the future applicability of our device in actual intersatellite communication systems.

Discussion

As discussed in the previous sections, the effective anti-phase RF current injected into the active layer in the fabricated device was much smaller than that applied at the top-side (n-side) electrodes, which resulted in a decrease in frequency change, Δf. By employing separated electrodes at the bottom side of the two-section PCSELs instead of the top side, a larger Δf can be realized with a much smaller amplitude of RF current. In this case, the optical phase change during one period of the RF signal during FM can be larger than π, even when the signal baud rate is further increased, and our FM PCSELs can also be used for phase shift keying (for example, binary phase shift keying (BPSK) and quadrature phase shift keying (QPSK)) (details are provided in Supplementary Section 8), the applicability of which has already been verified in several in-orbit demonstrations[24,26,27]. In addition,

by increasing the device size while reducing the coupling coefficients of the double-lattice photonic crystal, 10-W-class FM signal generation can also be realized (Supplementary Section 9). With these further improvements to increase the link budget and the signal baud rate, it will become possible to realize PCSEL-based ultra-small, one-chip, coherent transmitters for a wide variety of space communications, from intersatellite to deep-space communications.

In conclusion, towards the realization of optical-amplifier-free coherent FSO communications, we have demonstrated PCSELs that enable direct, high-power frequency modulation. We have proposed two-section PCSELs that incorporate two different photonic crystals with slightly different lattice constants, with which a large frequency change with well-suppressed AM signals can be generated via anti-phase RF current injection into the two sections. We have also performed a proof-of-concept experiment of coherent FSO communications using the two-section PCSEL, and we have demonstrated FSO communications with allowable power attenuations (link budgets) of 88 dB and 81 dB at signal baud rates of 0.5 Gbaud and 1.0 Gbaud, respectively, without using any optical amplifier. Importantly, our FM PCSELs are expected to enable the elimination of bulky and low-efficiency optical amplifiers and external modulators from transmitters in FSO communications, which is especially advantageous in intersatellite (LEO/GEO) communications, where the size, weight and power consumption of the transmitter should be made as small as possible. In addition, the above-mentioned link budgets and transmission rates can be further increased by optimizing the device structure to increase the average power and the amount of frequency change during modulation, which will enable even-longer-distance space communications such as Moon-to-Earth and deep-space communications. Such compact high-power coherent optical transmitters will also benefit other applications such as frequency-modulated continuous-wave LiDAR for

autonomous driving and atmospheric sensing[28,29]. We believe that our FM PCSELs will contribute to the development of one-chip, high-speed and high-efficiency optical transmitters for a wide variety of coherent free-space laser applications in the future.

Online content

Any methods, additional references, Nature Portfolio reporting summaries, source data, extended data, supplementary information, acknowledgements, peer review information; details of author contributions and competing interests; and statements of data and code availability are available at https://doi.org/10.1038/s41566-025-01782-2.

References

1. Uttam, D. & Culshaw, B. Precision time domain reflectometry in optical fibre systems using a frequency modulated continuous wave ranging technique. *J. Lightwave Technol.* **3**, 971–977 (1985).
2. Kikuchi, K. Fundamentals of coherent optical fibre communications. *J. Lightwave Technol.* **34**, 157–179 (2015).
3. Poulton, C. V. et al. Long-range LiDAR and free-space data communication with high-performance optical phased arrays. *IEEE J. Sel. Top. Quant. Electron.* **25**, 700108 (2019).
4. Rogers, C. et al. A universal 3D imaging sensor on a silicon photonics platform. *Nature* **590**, 256–261 (2021).
5. Kaushal, H. & Kaddoum, G. Optical communication in space: challenges and mitigation techniques. *IEEE Commun. Surv. Tutor.* **19**, 57–96 (2016).
6. Guiomar, F. P. M., Fernandes, A., Nascimento, J. L., Rodrigues, V. & Monteiro, P. P. Coherent free-space optical communications: opportunities and challenges. *J. Lightwave Technol.* **40**, 3173–3186 (2022).
7. Yamakawa, S. et al. LUCAS: the second-generation GEO satellite-based space data-relay system using optical link. In *Proc. 2022 IEEE International Conference on Space Optical Systems and Applications* 14–16 (IEEE, 2022).
8. Maho, A. et al. 100 W class output power transmission for high data rate, C-band, WDM free space optical ground-to-satellite links. In *Proc. 49th European Conference on Optical Communication (ECOC 2023)* 463–466 (IEEE, 2023).
9. Imada, M. et al. Coherent two-dimensional lasing action in surface-emitting laser with triangular-lattice photonic crystal structure. *Appl. Phys. Lett.* **75**, 316–318 (1999).
10. Riechel, S. et al. A nearly diffraction limited surface emitting conjugated polymer laser utilizing a two-dimensional photonic band structure. *Appl. Phys. Lett.* **77**, 2310–2312 (2000).
11. Hirose, K. et al. Watt-class high-power, high-beam-quality photonic-crystal lasers. *Nat. Photon.* **8**, 406–411 (2014).
12. Yoshida, M. et al. Double-lattice photonic-crystal resonators enabling high-brightness semiconductor lasers with symmetric narrow-divergence beams. *Nat. Mater.* **18**, 121–128 (2019).
13. Morita, R., Inoue, T., Zoysa, M. D., Ishizaki, K. & Noda, S. Photonic-crystal lasers with two-dimensionally arranged gain and loss sections for high-peak-power short-pulse operation. *Nat. Photon.* **15**, 311–318 (2021).
14. Inoue, T. et al. General recipe to realize photonic-crystal surface-emitting lasers with 100-W-to-1-kW single-mode operation. *Nat. Commun.* **13**, 3262 (2022).
15. Yoshida, M. et al. High-brightness scalable continuous-wave single-mode photonic-crystal laser. *Nature.* **618**, 727–732 (2023).
16. Noda, S. et al. High-power and high-beam-quality photonic-crystal surface-emitting lasers: a tutorial. *Adv. Opt. Photonics* **15**, 977–1032 (2023).
17. Morita, R. et al. Demonstration of high-power photonic-crystal surface-emitting lasers with 1-kHz-class intrinsic linewidths. *Optica* **11**, 333–339 (2023).
18. Ishimura, S. et al. Proposal and demonstration of free-space optical communication using photonic crystal surface-emitting lasers. *J. Lightwave Technol.* **41**, 3688–3694 (2023).
19. Orchard, J. R. et al. Small signal modulation of photonic crystal surface emitting lasers. *Sci. Rep.* **13**, 19019 (2023).
20. Morita, R. et al. High-speed high-power free-space optical communication via directly modulated watt-class photonic-crystal surface-emitting lasers. *Optica* **11**, 971–979 (2024).
21. Inoue, T. et al. Comprehensive analysis of photonic-crystal surface-emitting lasers via time-dependent three-dimensional coupled-wave theory. *Phys. Rev. B* **99**, 035308 (2019).
22. Katsuno, S. et al. Self-consistent analysis of photonic-crystal surface-emitting lasers under continuous-wave operation. *Opt. Express* **29**, 25118–25132 (2019).
23. Le, S. et al. 1.72-Tb/s virtual-carrier-assisted direct-detection transmission over 200 km. *J. Lightwave Technol.* **36**, 1347–1353 (2017).
24. Mahn, R. et al. Demonstration of an intradyne BPSK communication system with a GEO space ground link to the T-AOGS. In *Proc. 2023 IEEE International Conference on Space Optical Systems and Applications* 135–141 (IEEE, 2023).
25. Calvo, R. et al. Optical technologies for very high throughput satellite communications. *Proc. SPIE* **10910**, 109100W (2019).
26. Fields, R. et al. NFIRE-to-TerraSAR-X laser communication results: satellite pointing, disturbances, and other attributes consistent with successful performance. *Proc. SPIE* **7330**, 73300Q (2009).
27. Gregory, M. et al. Status on laser communication activities at Tesat-Spacecom. *Proc. SPIE* **12877**, 1287704 (2024).
28. Behroozpour, B., Sandborn, P. A., Wu, M. C. & Boser, B. E. Lidar system architectures and circuits. *IEEE Commun. Mag.* **55**, 135–142 (2017).
29. Lou, X., Feng, Y., Chen, C. & Dong, Y. Multi-point spectroscopic gas sensing based on coherent FMCW interferometry. *Opt. Express* **28**, 9014–9026 (2020).

¹Photonics and Electronics Science and Engineering Center, Kyoto University, Kyoto, Japan. ²Department of Electronic Science and Engineering, Kyoto University, Kyoto, Japan. ³KDDI Research Inc., Saitama, Japan. ⁴Chitose Institute of Science and Technology, Hokkaido, Japan. ⁵Kyoto University Institute for Advanced Study, Kyoto, Japan. ⁶These authors contributed equally: Takuya Inoue, Ryohei Morita. ✉e-mail: t_inoue@qoe.kuee.kyoto-u.ac.jp; snoda@qoe.kuee.kyoto-u.ac.jp

Methods

Calculation of beat note frequency change

To extract the instantaneous change in beat note frequency from the measured heterodyne waveforms, we first estimated the heterodyne offset frequency by taking a Fourier transform of the temporal waveform and finding the peak component. Next, we down-converted the waveforms to the baseband and filtered out-of-band noise. We then calculated the phase angles of the complex signals and extracted the instantaneous frequency change by evaluating the derivative of the phase angle with respect to time.

Evaluation of BER

Digital signal processing in the transmitter side involves generating a binary random signal using a 20-stage pseudo-random binary sequence (PRBS). This signal is then oversampled to two samples per symbol through zero-padding, and filtered with a raised-cosine filter that has a roll-off factor of 0. Subsequently, the signal is oversampled again to match the AWG sampling rate of 50 GS s^{-1}. At the receiver's offline digital signal processer, the frequency offset of the heterodyne beat signal is determined by locating the peak frequency component in its spectrum. The signal is then down-converted to the baseband using the identified negative frequency, and filtered to remove out-of-band noise. Frequency demodulation is accomplished by differentiating the phase angles of the baseband complex signals. Finally, the retrieved signal is equalized using the decision-directed least-mean-square (DD-LMS) algorithm, and the BERs are calculated by comparing the retrieved signal to the original 20-stage PRBS pattern. It should be noted that the eye pattern shown in Fig. 4b shows the dimensionless frequency data normalized to a range of [0, 1] after the above equalization process, and the line used to determine whether the data are 0 or 1 is the median (0.5) of the normalized data. As for the BER evaluation, we recorded the signal for 40 μs (corresponding to 20,000 bits at 0.5 Gbaud), and thus the detectable minimum BER was $1/20{,}000 = 5 \times 10^{-5}$.

Author contributions

S. Noda supervised the entire project with T.I., H.T., T.T. and M.S. T.I. designed the devices with R.M. and S. Nakano. R.M. and S. Nakano fabricated and characterized the samples with K.I. and M.D.Z. R.M. and S.I. performed the FSO experiments with T.I. All authors discussed the results and wrote the paper.

Competing interests

The authors declare no competing interests.

Additional information

Supplementary information The online version contains supplementary material available at https://doi.org/10.1038/s41566-025-01782-2.

Correspondence and requests for materials should be addressed to Takuya Inoue or Susumu Noda.

Peer review information *Nature Photonics* thanks the, anonymous, reviewers for their contribution to the peer review of this work.

Reprints and permissions information is available at www.nature.com/reprints.